J Mater Sci (2009) 44:1772–1779
DOI 10.1007/s10853-009-3253-x

Modeling of an oblique impact of solder droplet onto a groove with the impact point to be offset from the groove surfaces interface

Dewen Tian · Yanhong Tian · Chunqing Wang · Chunjin Hang

Received: 13 October 2008 / Accepted: 7 January 2009 / Published online: 7 February 2009

Abstract A three-dimensional VOF model has been developed to predict the oblique impact of a molten solder droplet onto a groove with the impact point to be offset from the groove surfaces interface. The contact angle boundary condition and the surface tension are considered in the present model. High speed videography system is used to record the impact dynamics. Asymmetric solder deformation is observed during the impact of the solder droplet onto the groove. The simulated results are in good agreement with the experiment. The presented model can accurately predict the characteristic geometry of the solder droplet, the interaction between the gas and the solder, the wall shear stress acting on the pads, and the energy variations during the impingement.

Introduction

Phenomena of droplet impact onto a solid surface can be encountered in many engineering applications, such as ink-jet printing, spray painting and coating, plasma spraying, rapid prototyping, solder jet bumping in chip packaging, etc. [1]. Spread and recoil are the most common phenomena encountered in the droplet impingements [2], whereas, many other phenomena may be encountered under special conditions, such as splash of droplet impingement on a coarse substrate with a high impact velocity [3, 4], evaporation and rebound on a hot substrate [5, 6], solidification on a cold substrate [7–9], etc. Droplet impingement, which is an extremely rapid process, is influenced by many factors and current researches are still insufficient to address the impinging mechanism.

There are lots of work reported on droplets impact on flat substrates including horizontal and inclined substrates [9–12] and the reports regarding non-flat substrates covering a tip of a pin projecting from a flat surface [13], a sharp edge [14], a spherical target [15], a substrate with a wavy surface [16], solidified droplet [17], a rough surface comprising microgrooves [18], etc. The author first reported the droplet impingement onto a groove [19]. The droplet impingement onto a groove is significantly influenced by the initial droplet impact position and direction. However, no related literature has been reported.

Numerical modeling, for its ability of process control and optimization and cost-minimizing effect, is continuously gaining importance. An accurate prediction of solder impingements may provide guidance to control and optimize the impingement process. The present numerical study focuses on the formation of spatial interconnection regarding the solder droplet impact on two perpendicular pads. An oblique impact model of a solder droplet onto a groove with the impact point to be offset from the groove surfaces interface has been developed to investigate the droplet shape evolution, energy variation, and interaction between the droplet and the pads. The visualization of the transient impact processes by a high speed videography system is employed to validate the numerical model.

Computational model

Control equations

The droplet impingement is solved using one-field volume of fluid tracking method which can model the motion of

D. Tian (✉) · Y. Tian · C. Wang · C. Hang
State Key Lab of Advanced Welding Production Technology, Harbin Institute of Technology, Harbin 150001, China
e-mail: tiandw@hit.edu.cn

two fluid phases. The mass and momentum conservation equations for Newtonian fluid under laminar flow conditions are given by

$$\nabla \cdot (\rho \vec{u}) = 0 \tag{1}$$

$$\frac{\partial}{\partial t}(\rho \vec{u}) + \nabla \cdot (\rho \vec{u}\vec{u}) = -\nabla p + \nabla \cdot [\mu (\nabla \vec{u} + \nabla \vec{u}^{\mathrm{T}})] + \rho \vec{g} + F_{\mathrm{VOF}} \tag{2}$$

where, ρ is the density, t is the time, $\vec{u}$ is the velocity vector, p is the pressure, μ is the viscosity, $\vec{g}$ is the gravitational acceleration vector, and F_{VOF} is the continuum surface force vector.

This single set of flow equations is used throughout the domain and mixture properties as defined below:

$$\phi = \alpha \phi_{\mathrm{l}} + (1 - \alpha)\phi_{\mathrm{g}} \tag{3}$$

where, ϕ is property variable, such as the density and viscosity; the subscript l and g represent liquid and gas phases, respectively; and α is the fraction of liquid phase.

In a particular computational cell: $\alpha = 0$: the cell is empty of the liquid; $\alpha = 1$: the cell is full of the liquid; $0 < \alpha < 1$: the cell contains the interface between the liquid and gas.

The tracking of the interface between the liquid and gas is accomplished by the solution of a continuity equation for the volume fraction of liquid.

$$\frac{\partial \alpha}{\partial t} + \vec{u}_{\mathrm{l}} \cdot \nabla \alpha = 0 \tag{4}$$

Surface tension is modeled as a smooth variation of capillary pressure across the interface. Following Brackbill et al. [20], it is represented as a continuum surface force (CSF) and is specified as a volumetric source term in the momentum equation as

$$F_{\mathrm{VOF}} = \sigma \frac{\rho \kappa \nabla \alpha}{1/2(\rho_l + \rho_g)} \tag{5}$$

where, σ is the surface tension coefficient, κ is the curvature, and defined in terms of the divergence of the unit normal $\hat{n}$ as

$$\kappa = \nabla \cdot \hat{n} = \frac{\nabla \alpha}{|\nabla \alpha|} \tag{6}$$

A piecewise-linear scheme from the work of Youngs [21] is used for the interface reconstruction. It assumes that the interface between two fluids has a linear slope within each cell, and this linear shape is used for the calculation of the advection of fluid through the cell faces.

Boundary conditions and numerical solution

The three-dimensional droplet impingement model is solved with the boundary conditions and the computational domain mesh as shown in Fig. 1. Only a half of the model is actually computed with a symmetric boundary. Constant pressure boundary condition is used in the simulation as the velocity profiles at these planes of the solution domain are not known. More attention should be focused on the treatment of wall adhesion and the movement of the contact line as the stress singularity will occur at the contact line if the traditional no-slip boundary condition at the wall is considered. When a droplet spreads on a solid surface, wall adhesion modifies the surface normal $\hat{n}$ as

$$\hat{\mathbf{n}} = \hat{\mathbf{n}}_w \cos(\theta) + \hat{\mathbf{t}}_w \sin(\theta) \tag{7}$$

where, $\hat{n}_w$ and $\hat{t}_w$ are the unit vectors normal and tangential to the wall, respectively, and θ is the contact angle at the wall. The local curvature of the surface is determined by the calculated surface normal of one cell away from the wall, and then this curvature is used to adjust the body force term in the surface tension calculation. Since it is difficult to measure the contact angles due to the complexity of droplet deformation, and the correlation for contact angle as a function of contact line velocity is not available in the literature, a constant contact angle $\theta = 140°$ is used as the liquid–solid contact angle.

Movement of the contact line on the wall surface may pose difficulties because a no-slip boundary condition is

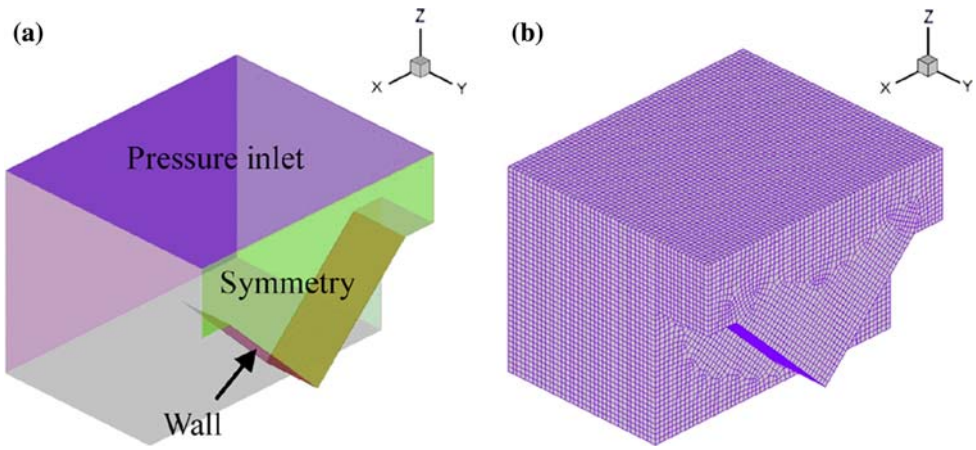

Fig. 1 **a** Boundary conditions and **b** computational domain mesh

Table 1 Materials properties used in the model

Properties	Solder	Gas
Density (kg/m)	7,500	1.225
Viscosity (Pa s)	0.002	0.0018
Surface tension coefficient (N/m)	0.431	

applied on the wall surface. However, in the present numerical implementation of the VOF model, the solid wall boundaries coincided with the cell boundaries. Though no-slip boundary condition was specified at the wall boundary (cell faces adjacent to the solid surface), the velocities at the cell center or other cell faces were not zero. Such non-zero velocities influenced the volume fraction and the position of the interfaces. Thus, the singularity is bypassed.

The system of model was solved with the boundary conditions using the commercial flow solver Fluent 6.3 (Fluent Inc.) Mass and momentum equations were solved using a second-order implicit method for space and a first-order implicit method for time discretization. Pressure interpolation was performed using a body-weighted scheme. This scheme is useful when the body force is comparable to the pressure force. Body force-weighted pressure interpolation assumes continuity of ratio of gradient of pressure and density. This ensures that any density-weighted body force is balanced by pressure. Pressure implicit with splitting of operator (PISO) was used for pressure velocity coupling in the momentum equation. This scheme was used to reduce the internal iteration per time step and larger under relaxation parameters can be used. The impact velocity is $u_x = 0.1$ m/s, $u_y = 0$ m/s, $u_z = -1.0$ m/s, and the initial impact position is 0.5 mm offset to the left from the center. The material properties used in the model are listed in Table 1.

Experimental methods

To validate the numerical model, a new apparatus was used for capturing the droplet images during the droplet impingement. The main components are the translation stage, the solder droplet generator, the gas chamber, the *x*–*y* precision work stage, and the high speed videography system with data acquisition capability. A schematic representation of the experimental setup is shown in Fig. 2. A temperature control unit affiliated to the solder droplet generator was used to heat the Sn3.0Ag0.5Cu solder to the molten state and then a pressure-driven unit was used to squeeze a molten solder droplet out of the nozzle. The droplet fell into the chamber filled with Argon and then impacted on the substrate which was on an *x*–*y* working stage. The falling height can be adjusted to achieve a desired impinging velocity. Different impact direction can be obtained by adjusting the substrate inclination. The rapid motion involved in the solder impingement was captured with EPIX video acquisition system with maximum speed of 955 frames per second. The pads were formed with a 2 mm × 6 mm rectangle-shaped copper foil which was folded into two perpendicular pads. Then the pads were placed in the groove of a plastic substrate. The initial droplet temperature was 300 °C which was about 80 °C above the solder melting point. No solidification was observed in the experiment. Therefore, the heat transfer was not considered in the numerical model.

Results and discussion

Shape evolution during droplet impingement

To describe the solder geometry quantitatively and to obtain the flow information in the specific directions during the impingement, we defined two cross section (*X*–*Z* and *Y*–*Z*) and five characteristic geometry variables (L_l, L_r, L, W, H), as shown in Fig. 3. The W was defined using the concept of maximum spread as the flow in y direction would be out of the range of the pads; whereas, L_l and L_r were defined with the position of the contact line as the flow in the X direction always remains within the edge of the pads. To impart a measure of generality, the characteristic geometry variables defined above were made dimensionless using the initial droplet diameter d_0, and the velocities using the impact velocity V_0, as $L_l^* = L_l/d_0$, $L_r^* = L_r/d_0$, $L^* = L/d_0$, $W^* = W/d_0$, $H^* = H/d_0$, $V^* = V/V_0$.

Figure 4 shows the temporal evolution of the solder droplet impacting onto the perpendicular pads. When a solder droplet impacts onto the left pad, the front edge of the droplet spreads forward and the back edge spreads backward. Though the impact direction of the droplet is not normal to the left pad, the droplet spreads approximately symmetrically with respect to the impacting point at the beginning stage ($t = 1.1$ ms). When the front edge of the droplet reaches the right pad, the spread shows asymmetric features to the impacting point. Moreover, the solder will accumulate at the spread edge ($t = 2.1$ ms) as the bulk flow velocity is greater than that of the contact line region for the wall adhesion. The back edge of the droplet recedes and slips forward when the droplet reaches its maximum spread. Protrusion is formed in the y direction with a weak constraint ($t = 3.1$ ms). The end of the protrusion is sphere-like and becomes smooth with increase in time. The droplet is then elongated and move towards the right pad ($t = 4.1$ ms, $t = 5.1$ ms).

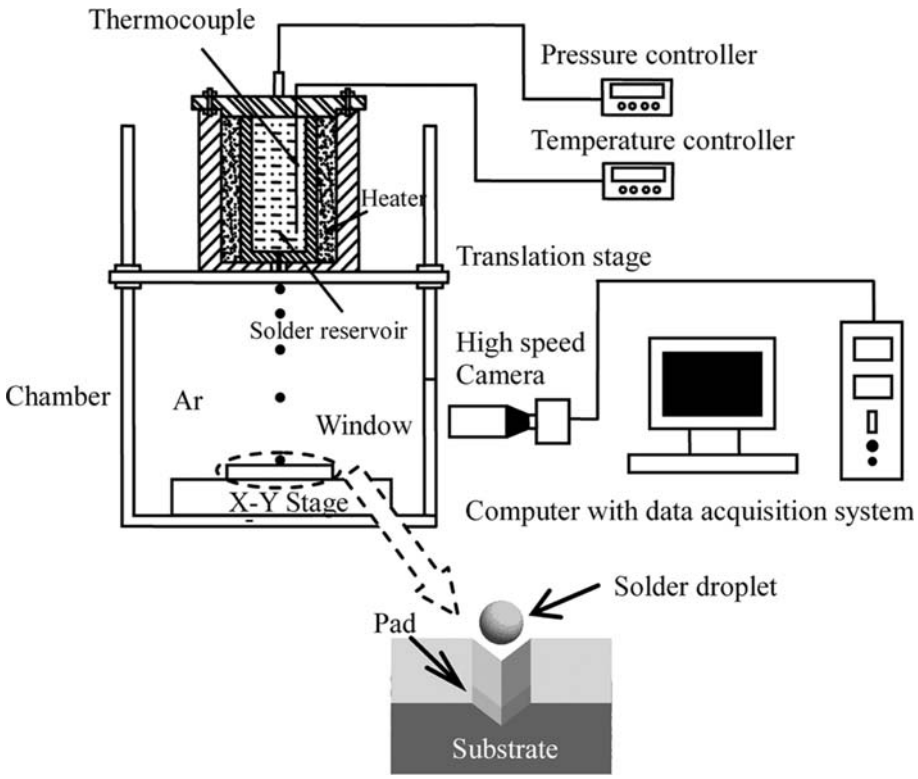

Fig. 2 Schematic diagram of the experimental setup

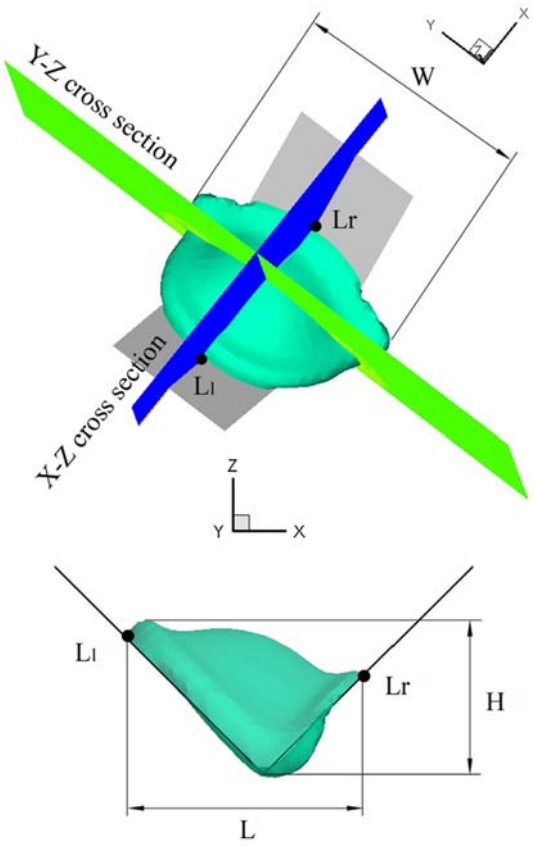

Fig. 3 Definition of cross sections and geometry variables

The modeling results are in good agreement with the photographs by comparing the results in the 1st and 2nd columns of Fig. 4. As can be seen from the *Y–Z* and *X–Z* cross sections, the regions of the droplet in contact with the pad have relatively high pressures. Firstly, the high pressure location is at the left pad interface and then is transferred to the right pad interface. The pressure decreases with the proceeding of the impingement.

Figure 5 shows the quantitative geometry evolution during the droplet impingement. Three characteristic time points: t_1, t_2, and t_3, which are labeled in the horizontal axis, present the time when solder reaches the pad edges in y direction, the time for the front edge of droplet approaching the right pad, and the time for the solder reaching its maximum spread in the x direction ($L^*_{\max}$), respectively. Within the time range of 0–t_2, the front edge of the droplet moves forward slowly, and then spreads rapidly as it touches the right pad. The subsequent receding is relatively slow. The back edge recedes earlier than that of the front edge. In addition, the spread velocity and the final deformation in the y direction are much greater than those in the x direction.

The interaction between the ambient gas and droplet determines the droplet shape as the gas recirculatory motion has great influence on the droplet shape. The recirculatory motion can be quantified by calculating the vorticity ω as

$$\omega = \nabla \times \vec{u} \tag{8}$$

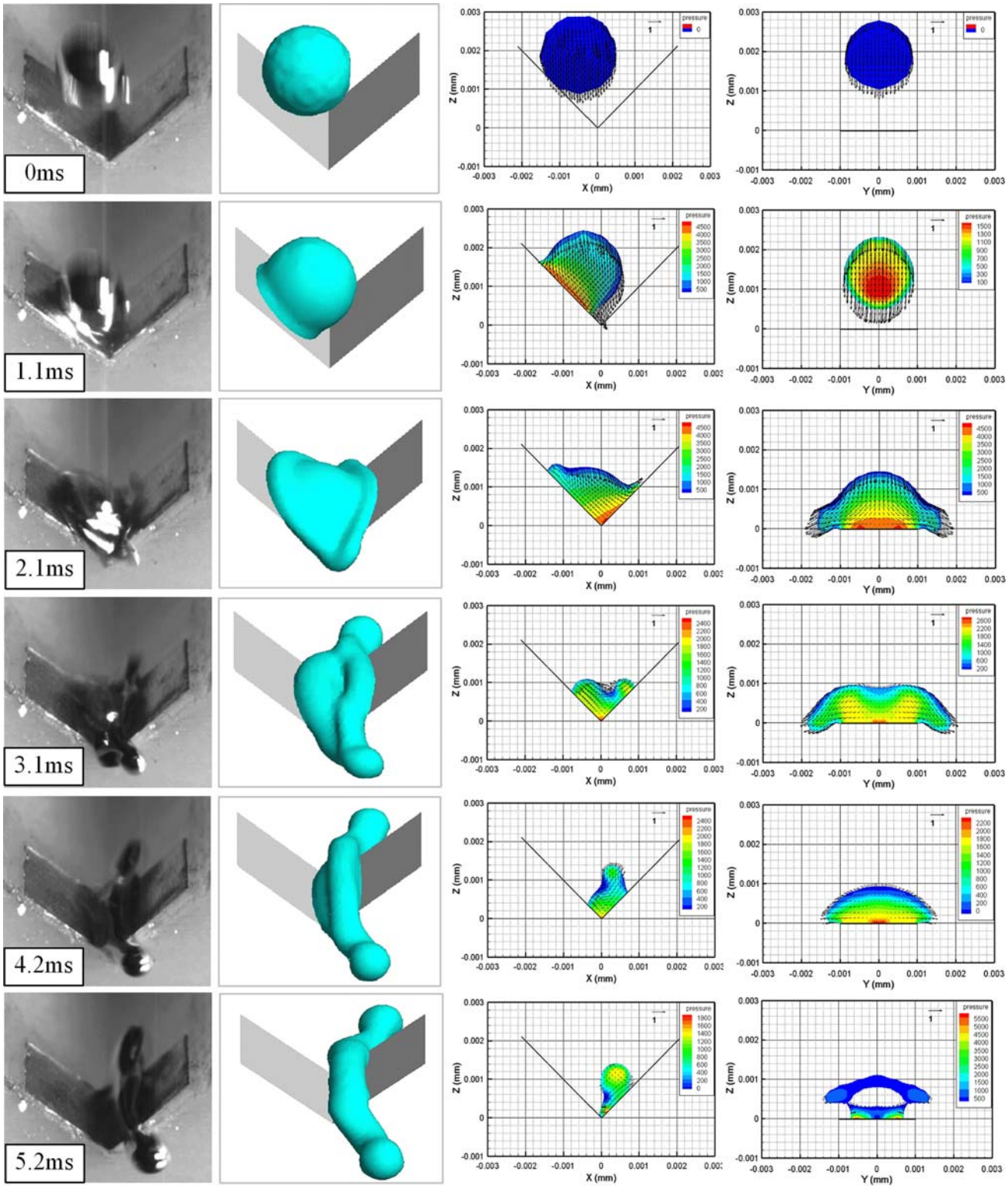

Fig. 4 Time evolution of solder droplet impact on two perpendicular pads (1st column: photographs; 2nd column: computer generated images; 3rd column: pressure contour and velocity vectors in *X–Z* cross-section; 4th column: pressure contour and velocity vectors in *Y–Z* crosssection)

Figure 6 shows the vorticity and strain rate contours of droplet surface. The vorticities at the spreading edge and intermediate ridges are relatively high. High strain rate is observed in the vicinity region with the high gas vorticity. It can be concluded that high vorticity/strain rate occurs at the region where the shape has an abrupt change.

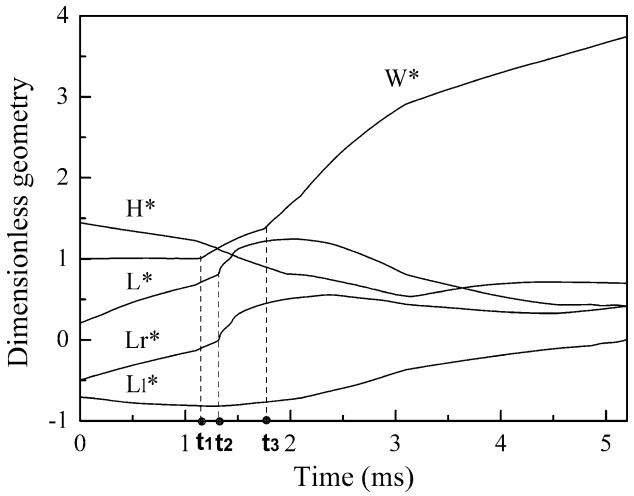

Fig. 5 Evolution of the characteristic geometry during the impingement

Interaction between the solder droplet and the pads

The interaction between the droplet and pads can be evaluated quantitatively by the shear stress exerted by the flowing solder fluid over the pad surface. Figure 7 shows the shear stress distribution on the pads at different moments during the droplet impingement. As the droplet touches the pads, the solder spreads downward along the pads easily under the gravitational effect. The velocity gradient downward along the pads is greater than that in any other directions. The region of maximum shear stress has a meniscus shape before the droplet reaches the pad interface ($t = 1.1$ ms). The meniscus moves towards and then meets the interface of the pads ($t = 1.35$ ms). When the solder spreads to the pad edges in y direction, the high shear stress region transfers to the pad edges ($t = 2.1$ ms). After that, the high walls shear stress region is switched from the left spread edge to the pad edges with the receding of the solder ($t = 3.1$ ms, $t = 4.2$ ms) and finally it reaches at the back edge of the solder ($t = 5.2$ ms). In conclusion, the maximum stress is always located in the vicinity of the contact line region which has the maximum velocity gradient during the impingement. The value of the maximum shear stress decreases with the increase in time.

The area-weighted averaged stress variation with time is shown in Fig. 8. It can be found that the maximum averaged stress of the left pad occurs at the moment t_2, which corresponds to the instant when the front edge of the solder meets the pads interface. The maximum averaged stress of the right pad occurs at the moment $t = 1.67$ ms. When the solder reaches the right pad, the average velocity of the bulk flow decreases. Therefore, the maximum average shear stress of the left pad (τ_{lmax}) is bigger than that of the right pad (τ_{rmax}).

Energy analysis of droplet impingement

The droplet impingement is actually a process of the energy transformation which involves the gravitational potential energy, the kinetic energy, the surface energy, and the viscous dissipation. Each energy component can be calculated by the modeling results. The surface energy SE can be described as

$$SE = S_{\mathrm{gl}}\sigma_{\mathrm{gl}} + S_{\mathrm{ls}}(\sigma_{\mathrm{ls}} - \sigma_{\mathrm{gs}}) \tag{9}$$

where, S_{gl} and S_{ls} are the gas–liquid and liquid–solid interface areas, respectively; σ_{ls}, σ_{gs}, and σ_{gl} are the interfacial tensions of the liquid–solid, gas–solid, and gas–liquid interfaces, respectively.

σ_{ls} can be obtained from the Young's equation

$$\sigma_{\mathrm{gs}} = \sigma_{\mathrm{ls}} + \sigma_{\mathrm{gl}}\cos\theta_{\mathrm{e}} \tag{10}$$

where, θ_{e} is the equilibrium contact angle.

Substituting (10) into (9), we can get

$$SE = \sigma_{\mathrm{gl}}(S_{\mathrm{gl}} - S_{\mathrm{ls}}\cos\theta_{\mathrm{e}}) + S_0\sigma_{\mathrm{sg}} \tag{11}$$

where, S_0 is the pad area. The last term $S_0\sigma_{\mathrm{sg}}$ in Eq. 11 remains constant during the droplet impingement. It has no contribution to the energy variation during the impingement and can be neglected. Then the surface energy is described as

$$SE = \sigma_{\mathrm{gl}}(S_{\mathrm{gl}} - S_{\mathrm{ls}}\cos\theta_{\mathrm{e}}) \tag{12}$$

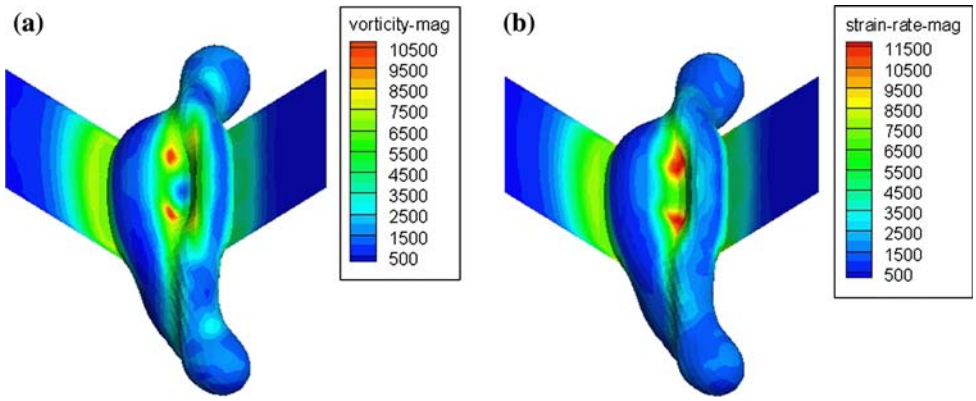

Fig. 6 Distribution of **a** vorticity and **b** strain rate at the moment $t = 3.1$ ms

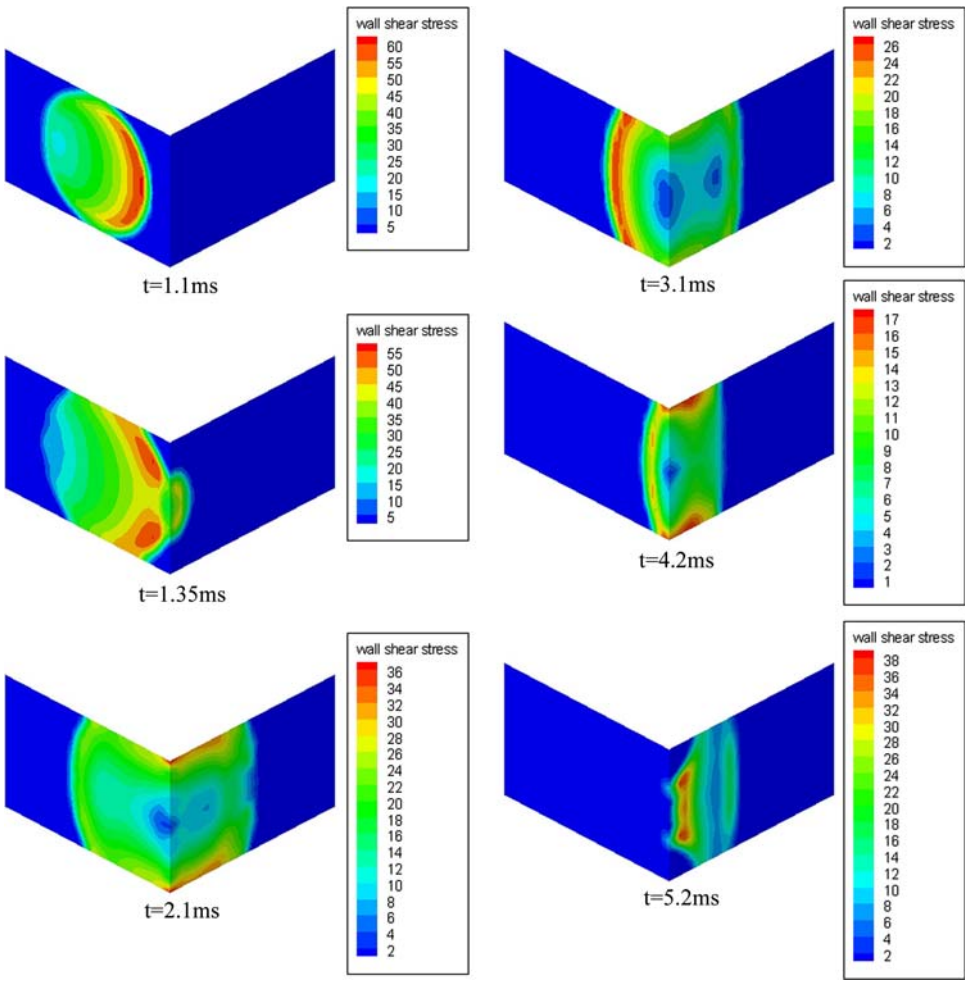

Fig. 7 Evolution of wall shear stress of the pads during the droplet impingement

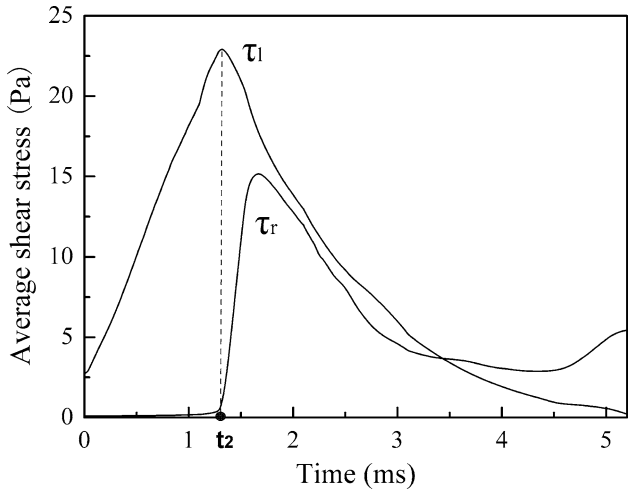

Fig. 8 Area-weighted average shear stress of pads as a function of time

The gravitational potential energy *GE* and the kinetic energy *KE* can be achieved using the integral over the whole computational domain *D* as

$$GE = \iiint_D (\rho_l g z \alpha) \mathrm{d}V \tag{13}$$

$$KE = \iiint_D \left(\frac{1}{2}\rho_l V e^2 \alpha\right) \mathrm{d}V \tag{14}$$

where, $Ve = (u_x^2 + u_y^2 + u_z^2)^{1/2}$, u_x, u_y, and u_z are the velocity components at x, y, and z directions, respectively.

The viscous dissipation *VD* is calculated using the energy balance method as

$$SE^0 + GE^0 + KE^0 = SE + GE + KE + VD \tag{15}$$

where, the superscript 0 denotes quantities evaluated at the initial condition ($t = 0$).

Figure 9 shows the energy evolution during the droplet impingement. The decrease of gravitational potential energy during the whole impingement process is very small and can be neglected. Before the front edge of the solder reaches the right pad ($t = t_2$), each energy component varies slowly. And then, they change rapidly. Within the time range 0–5 ms, the kinetic energy decreases monotonically, the viscous dissipation increases monotonically, whereas the surface energy varies non-monotonically.

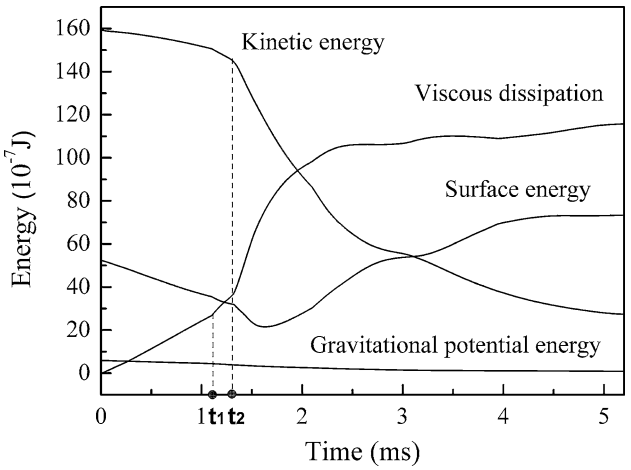

Fig. 9 Energy variation with time

During the late stage of the impingement, the variation of each the energy component is small.

Conclusions

A three-dimensional numerical model has been developed to predict the asymmetric deformation of droplet obliquely impacting onto a groove with an impact position to be offset from the pads interface. The model is based on fixed-grid algorithm with a VOF scheme to track the solder surface. Surface tension is modeled as a volume force acting on the fluid in the vicinity of the free surface using the CSF algorithm. A contact angle is specified as a boundary condition along the contact line.

High speed videography system is used to observe the droplet impact. It is found that the front edge of the droplet spreads forward and the back edge spreads backward as the solder droplet impacts onto the left pad. Subsequently, the back and front edges of the droplet recede in turn. The droplet deforms easier in *y* direction and finally outflows from the pad to form protrusions with smooth sphere-like end. The simulated results agree well with the experimental. The interaction between the gas and solder shows that the high vorticity or high strain rate occurs at the region with an abrupt shape change of the solder surface. The shear stress distribution on the pads indicates that the contact line region has the maximum velocity gradient. The kinetic energy, the surface energy, and viscous dissipation are the main energy components during the impingement. The gravitational potential energy is small and can be neglected. The energy dramatically changes when the solder approaches the right pad.

Acknowledgements This research is supported by the National High-tech R&D Program (863 Program) of China, Grant No. 2007AA04Z314.

References

1. Yarin AL (2006) Annu Rev Fluid Mech 38:159
2. Gunjal PR, Ranade VV, Chaudhari RV (2005) AIChE J 51:59
3. Xu L, Zhang WW, Nagel SR (2005) Phys Rev Lett 94:184505
4. Shakeri S, Chandra S (2002) Int J Heat Mass Transf 45:4561
5. Nikolopoulos N, Theodorakakos A, Bergeles G (2007) Int J Heat Mass Transf 50:303
6. Yang G, Liang-Shih F (2006) J Chin Inst Chem Eng 37:71
7. Waldvogel JM, Poulikakos D (1997) Int J Heat Mass Transf 40:295
8. Zadrazil A, Stepanek F, Matar OK (2006) J Fluid Mech 562:1
9. Wang W, Hong F, Qiu H (2006) IEEE Trans Compon Packag Technol 29:486
10. Lunkad SF, Buwa VV, Nigam KDP (2007) Chem Eng Sci 62:7214
11. Kamnis S, Gu S (2005) J Phys D Appl Phys 38:3664
12. Xue M, Heichal Y, Chandra S et al (2007) J Mater Sci 42:9. doi: 10.1007/s10853-006-1129-x
13. Azar RG, Yang Z, Chandra S et al (2005) Int J Heat Fluid Flow 26:334
14. Bussmann M, Mostaghimi J, Chandra S (1999) Phys Fluids 11:1406
15. Bakshi S, Roisman IV, Tropea C (2007) Phys Fluids 19:032102
16. Ahmed AM, Rangel RH (2002) Int J Heat Mass Transf 45:1077
17. Haferl S, Poulikakos D (2002) J Appl Phys 92:1675
18. Kannan R, Sivakumar D (2008) Exp Fluids 44:927
19. Tian DW, Tian YH, Wang CQ et al (2008) J Phys D Appl Phys 41:245503
20. Brackbill JU, Kothe DB, Zemach C (1992) J Comput Phys 100:335
21. Youngs DL (1982) Numer Meth Fluid Dyn 1:41